Bond Behaviour between Hybrid Fiber Reinforced Polymer Sheets and Concrete

Cheng Yuan[1], Wensu Chen[1], Thong M. Pham[1], Hong Hao[1,2]*

[1]Centre for Infrastructural Monitoring and Protection
School of Civil and Mechanical Engineering, Curtin University, Australia
Kent Street, Bentley, WA 6102, Australia
[2]School of Civil Engineering, Guangzhou University, Guangzhou 510006, China,
**Corresponding Author*

Abstract

Fibre reinforced polymer (FRP) has been used for strengthening concrete structures. Debonding has been identified as one of the most common failure modes of such composite structures. Numerous studies have been conducted to investigate the bond behavior between FRP and concrete. Hybrid FRP, which is made of combinations of different types of fibers, has shown their excellent performance in strengthening structures. However, only limited studies have been conducted on the bond behaviour between hybrid FRPs and concrete. This study investigates the interfacial behaviour between hybrid FRP (carbon/basalt) and concrete blocks by using the single-lap shear testing method. The digital image correlation (2D-DIC) technique is used to measure the full fields of displacements and strain of the specimens. The effects of FRP stacking order and the mechanical properties of FRP on the bond behavior are evaluated. The experimental results show that the FRP stacking order has obvious influences on the debonding load and the bond-slip relationship. The effect of FRP stacking order on the fracture energy is also examined. The existing models are recalibrated with consideration of stiffness variations and the predictions of the modified models agree better with the experimental results.

1. Introduction

Fibre reinforced polymer (FRP) has been used for strengthening concrete structures due to its low weight and high strength [1-4]. Glass fibre (GFRP) and carbon fibre (CFRP) are the most common FRP composites used in industry. Basalt fibre (BFRP) has been increasingly used as a FRP composite owing to its superior characteristics such as high strength to weight ratio and cost effectiveness [5, 6]. As reported, debonding of FRP from the concrete substrates is the primary failure mode at the interface between FRP and concrete due to high stress concentrations [7-9]. The interfacial bond behavior of FRP-to-concrete is critical for preventing debonding failures in FRP-strengthened concrete structures [10-14]. The interfacial bond capacity between FRP and concrete is mainly influenced by the mechanical properties of concrete substrates, mechanical properties of adhesive, and stiffness of FRP [15-17]. Most previous shear bonding tests focused on a single type of FRP (e.g. CFRP or GFRP) to investigate the bond behavior between FRP and concrete [7, 10, 11, 15, 16, 18-26].

In order to improve the utilization of FRP composites and the ductility, hybrid FRPs have been used to strengthen concrete structures. Grace et al. [27] developed a uniaxial ductile hybrid FRP fabric composed of two types of carbon fibres and one type of glass fibre. An experimental study on eight concrete beams strengthened by the hybrid FRPs was carried out. It was found that the beams strengthened with hybrid fabric can obtain higher ultimate strength and ductility as compared to those beams strengthened with sole CFRP systems. Grace et al. [27] also developed a new pseudo-ductile FRP fabric composed of CFRP and GFRP with three different angles (0°, 45°, and -45°). A ductile plateau in load-displacement curves similar to steel reinforcement was observed. Li et al. [28] numerically simulated the debonding process between carbon fibre sheet and the glass fibre sheet (CFRP-GFRP) as well as CFRP-CFRP and GFRP-GFRP. The numerical results showed that it was an effective method for CFRP-GFRP hybrid sheets to strengthen concrete substrates due to the fact that hybrid FRPs can effectively reduce interfacial shear stresses of FRP sheets. Choi et al. [29] conducted experimental and analytical studies on the debonding of hybrid FRPs for strengthening reinforced concrete (RC) beams. The experimental results showed that the beams strengthened with stiffer FRP had higher debonding strength than the beams strengthened with less stiff FRP and the beam strengthened with thinner FRP had higher debonding strength than the beam strengthened with thicker FRP. Hawileh et al. [30] experimentally and analytically studied the flexural performance of RC beams with different combinations of CFRP and GFRP sheets. The hybrid FRPs combining the GFRP sheets of lower stiffness with the CFRP sheets of higher stiffness were used to provide an improved strength and ductility in beams. The beams strengthened with GFRP sheets and hybrid FRP sheets were more ductile than that strengthened with sole CFRP sheets.

To better understand the mechanical behaviours of hybrid FRPs strengthened concrete structures, an experimental investigation was conducted in this study to investigate the bonding behaviors between hybrid FRPs and concrete blocks by using the method of single-lap shear tests as the single shear test is a common and reliable testing method in the literature [31-33]. Relatively high tensile strength carbon fibre (CFRP) and relatively ductile basalt fibre (BFRP) with different number of layers were used to compose the hybrid FRP fabrics. The key parameters considered in this study were FRP type, FRP stacking order and FRP stiffness. The digital image correlation technique ARAMIS® (GOM Correlate 2D software) was used in this study to measure the full-fields of displacements and strain of the specimens. The bond-slip relationships of hybrid FRPs were obtained from strain distributions during loading processes. Meanwhile, a fitting procedure was proposed and verified to obtain the bond-slip curves. Simplified bond-slip curves for hybrid FRP-to-concrete were proposed in this study and compared with the bond-slip curves predicted by two existing bond-slip models.

2. Experimental program

2.1 Material properties

Concrete blocks with length of 350 mm, width of 150 mm and height of 150 mm were prepared as substrates. Coarse aggregates with the size of 5~20 mm and fine aggregates of silica-based river sand were used in preparing the concrete blocks. The concrete blocks were demolded 24 hours after casting and then cured in water tank for 28 days. The average compressive strength of three concrete cylinders was f_c = 39.68 MPa.

The polymer matrix used to saturate the fibre was a mixture of epoxy resin (West System 105) and hardener at a ratio of 5:1. The epoxy resin had a tensile strength of 50.5 MPa, tensile modulus of 2.8 GPa and rupture tensile strain of 4.5% [5, 34]. Unidirectional basalt fibre and carbon fiber had the same unit weight of 300 g/m^2. The material tests of CFRP and BFRP were conducted according to ASTM D3039 [35] and the material properties are listed in Table 1.

Table 1

Mechanical properties of FRP materials

Material	Tensile strength (MPa)	Young's modulus (GPa)	Rupture strain (%)	Nominal thickness (mm)
CFRP	1990	191	1.04	0.167
BFRP	1333	71	1.70	0.120

2.2 Specimens preparation

A total of 24 specimens were prepared for this experiment. Figure 1 shows the details of the specimens. To investigate the effect of the FRP type, FRP stacking order and FRP stiffness on the bonding behavior, different layers of FRP (CFRP and BFRP) with the bonded width of 40 mm and the bonded length of 200 mm were prepared with epoxy resin on one side of the concrete blocks along the axial direction. The concrete surface was prepared with a needle scaler to remove the vulnerable mortar and expose the aggregates. After removing dust, FRP sheets of different layers were bonded onto the concrete blocks. The specimens are divided into three groups as defined in Table 2. The first group was designed to study the effect of FRP types on the bonding behavior. The second and third groups were designed to examine the effects of stacking order and FRP stiffness on the bonding behavior, respectively. The name of the specimens includes three parts, the first part is the order of the group, the second and third parts indicate the number of CFRP and/or BFRP layers, respectively. For example, G3_1C4B represents that the specimen belongs to group 3, and has one layer of CFRP (named 1C) attached to the concrete block and four layers of BFRP (named 4B). To reduce the uncertainties, at least three specimens (i.e. 1, 2, 3) were prepared for each configuration.

2.3 Prediction of elastic modulus of hybrid FRPs

The modulus of elasticity of the hybrid FRP sheets (i.e. 1C1B, 1B1C, 1C4B and 4B1C) can be measured in the testing using equation (1) and also predicted from the rule of mixtures using equation (2) [36, 37]:

$$E_H = \frac{f_{HF}}{\varepsilon_{HF}} \tag{1}$$

$$E_H = \frac{E_B t_B + E_C t_C}{t_B + t_C} \tag{2}$$

where E_H = elastic modulus of hybrid FRPs, f_{HF} is the experimental tensile stress of hybrid FRPs, ε_{HF} is the experimental rupture strain of hybrid FRPs, E_B = elastic modulus of BFRP sheet, E_C = elastic modulus of CFRP sheet, t_B = thickness of BFRP sheet, and t_C = thickness of CFRP sheet. These two equations, however, do not necessarily give the same estimations of the hybrid FRP sheet. For example, the elastic modulus of G2_1B1C is predicted by Equation (2) as 141 MPa, which is however different from the results of the coupon tests (121 MPa). The cause of this discrepancy is explained below. When the hybrid carbon-basalt FRP sheet was subjected to loading, the CFRP layer of relatively higher elastic modulus and lower ultimate strain ruptured first followed by the rupture of BFRP layer, as shown in Figure 2. It is found that the rupture strain of hybrid specimen is enhanced due to the hybrid effect, which is consistent with the findings in the literature [37, 38]. Manders and Bader [37] reported that the rupture strain of laminated hybrid carbon-glass FRPs was about 50% higher than that of single CFRP. Aveston and Sillwood [38] found that the strain of hybrid carbon-glass composites at CFRP rupture increased by 30%. In this study, the rupture of hybrid sheet 1C1B and 1C4B both initiated at CFRP layer and the rupture strain of CFRP layer is 1.36% and 1.50%, respectively, which is higher than the rupture strain of 1.04% for single sheet 1C, as shown in Figure 2. If Equation (2) is used to calculate the elastic modulus, it leads to over prediction because the actual rupture strain for hybrid sheet ε_{HF} is higher than that of the single sheet ε_C .

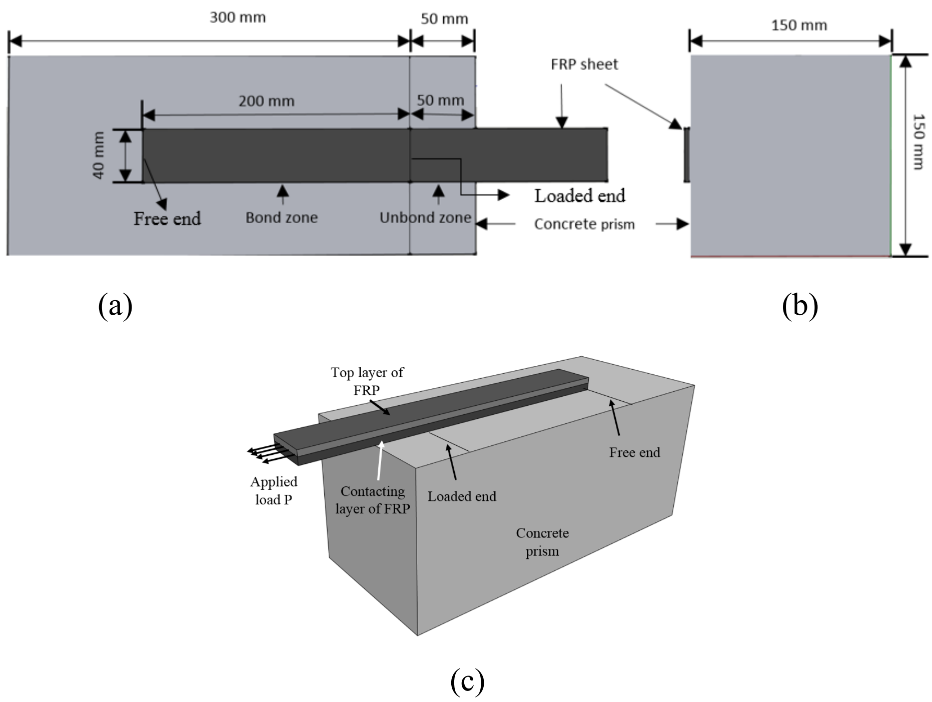

Figure 1. Scheme of single-lap shear specimen (a) front view; (b) side view; (c) 3D view

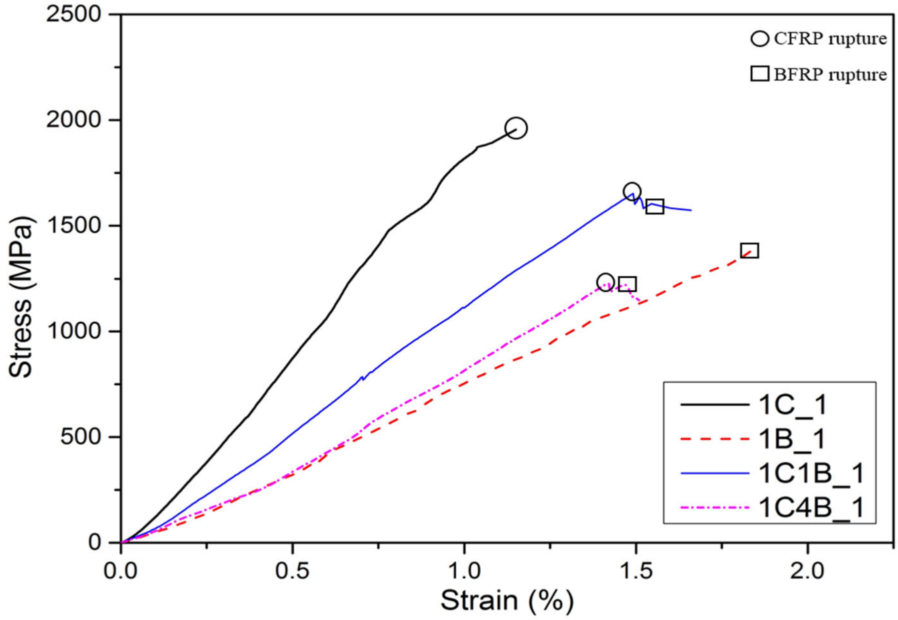

Figure 2. Experimental stress and strain of FRP sheet

Table 2. Testing scheme and specimen parameters

Specimen	Nominal thickness (mm)	Tensile strength (MPa)	Rupture strain (%)	Elastic modulus (GPa)	FRP stiffness (N/mm)	Predicted elastic modulus (MPa)
			Group one			
G1_1B_1, 2, 3	0.120	1333	1.71	71	8.52	N/A
G1_1C_1, 2, 3	0.167	1990	1.04	191	31.90	N/A
			Group two			
G2_1B1C_1, 2, 3	0.287	1644	1.36	121	34.73	141
G2_1C1B_1, 2, 3	0.287	1644	1.36	121	34.73	141
G2_1B1B_1, 2, 3	0.240	1459	1.81	80	19.20	71
G2_1C1C_1, 2, 3	0.334	1908	1.19	160	49.43	179
			Group three			
G3_1C4B_1, 2, 3	0.647	1277	1.50	85	54.99	102
G3_4B1C_1, 2, 3	0.647	1277	1.50	85	54.99	102

Note: The data is averaged from three specimens

2.4 Testing setup

The single-lap shear tests were carried out using the Shimadzu AGS-X 50KN Series universal testing machine in Curtin University as shown in Figure 3. All the specimens were tested in displacement control at a loading rate of 0.3 mm/min [39]. The machine was equipped with an inbuilt load cell to measure the load during the tests. Two strain gauges with 5 mm gauge length were mounted onto the surface of FRP sheets to measure the strain. The strain gauge 1 (SG1) was mounted at a distance of 10 mm from the bonded area. The strain gauge 2 (SG2) was mounted at a distance of 60 mm from the unbonded area as shown in Figure 3.

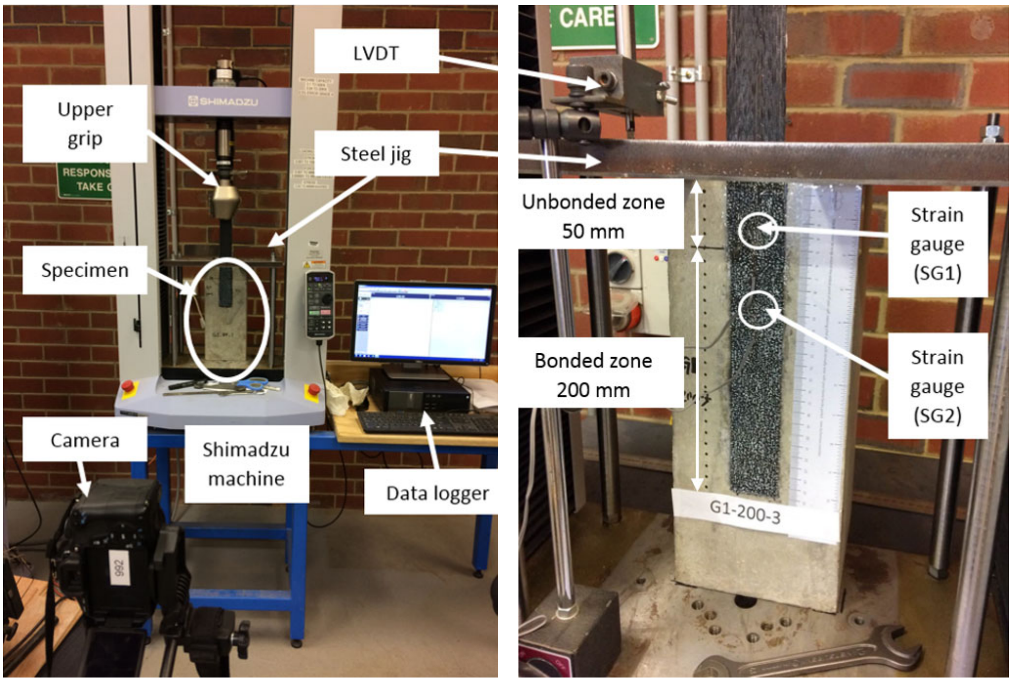

Figure 3. Shimadzu AGS-X 50KN testing machine (L) Setup; (R) Schematic diagram

3. Experimental results and discussion

3.1 Failure mode

Two typical failure modes were observed in this study: debonding failure within a thin layer of concrete and FRP rupture. The specimens G1_1B_2, G1_1B_3, and G1_1C_2 experienced the FRP rupture failure. As shown in Figure 4 (a), the rupture failure occurred near the clamp area of the loading machine. For the specimens 1B and 1C, the ultimate bonding strength between FRP and concrete is close to the tensile strength of FRP, which could result in either debonding failure or FRP rupture. For instance, the rupture strength of one layer of BFRP sheet 1B is calculated as 6.3 kN, which is close to the ultimate bonding strength of 5 kN. For the one-layer-CFRP 1C, the rupture strength is calculated as 13.2 kN which is close to the ultimate bonding strength of 12 kN. Except the specimens G1_1B_2, G1_1B_3, and G1_1C_2, the rest of the specimens experienced debonding failure, and all the debonding initiated at the loaded end for all the specimens, which is consistent with the results in the previous studies [40-42]. The photographs of rupture failure of specimen G1_1B_2 and debonding failure of specimen G2_1C1B_2 after the tests are shown in Figure 4. The variations in stiffness and stacking order of hybrid FRPs have no effect on the failure modes of hybrid FRPs-concrete interface.

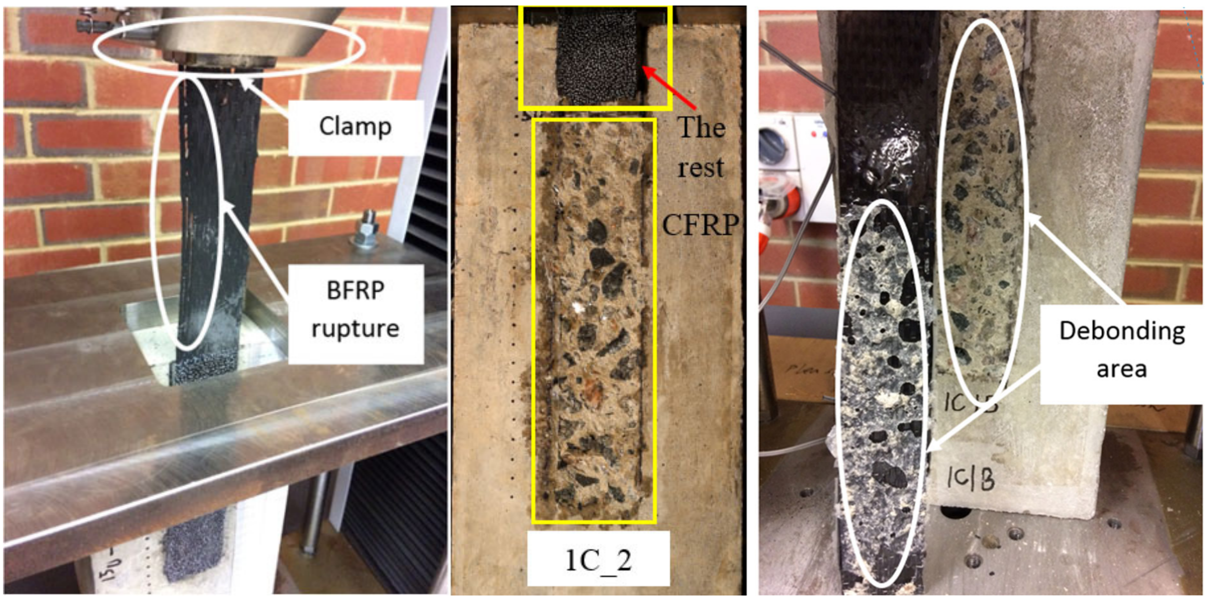

(a) FRP rupture (b) FRP debonding

Figure 4. Failure modes of specimens

3.2 Load and displacement

Figure 5 shows the experimental results of load-displacement graphs. Most of the testing results are consistent for each configuration. The measured displacement includes the shear slip of the bonded part and the elongation of the unbonded part of FRP sheets similar to the testing presented in the previous study [40]. The load-displacement curves of the specimens G1_1B_2, G1_1B_3, and G1_1C_2 experiencing FRP rupture failure were also plotted herein for completeness. As observed, the bonding strength is greatly affected by the FRP stiffness and stacking order. The average bonding strength of the specimens G1_1B, G2_2B, G1_1C, G2_1B1C, G2_1C1B, G2_2C, G3_1C4B, and G3_4B1C is 4.61, 7.17, 9.00, 11.91, 13.10, 13.85, 13.96, and 17.53 kN, respectively. As shown in Figure 6, the bonding strength increases with the stiffness of FRP sheet, which is also consistent with the previous studies [2, 43]. For the specimens G2_1C1B/G2_1B1C with the same stiffness of FRP but different stacking order, the bonding strength are different and the variation may be resulted from the difference in the stiffness of the contacting layer.

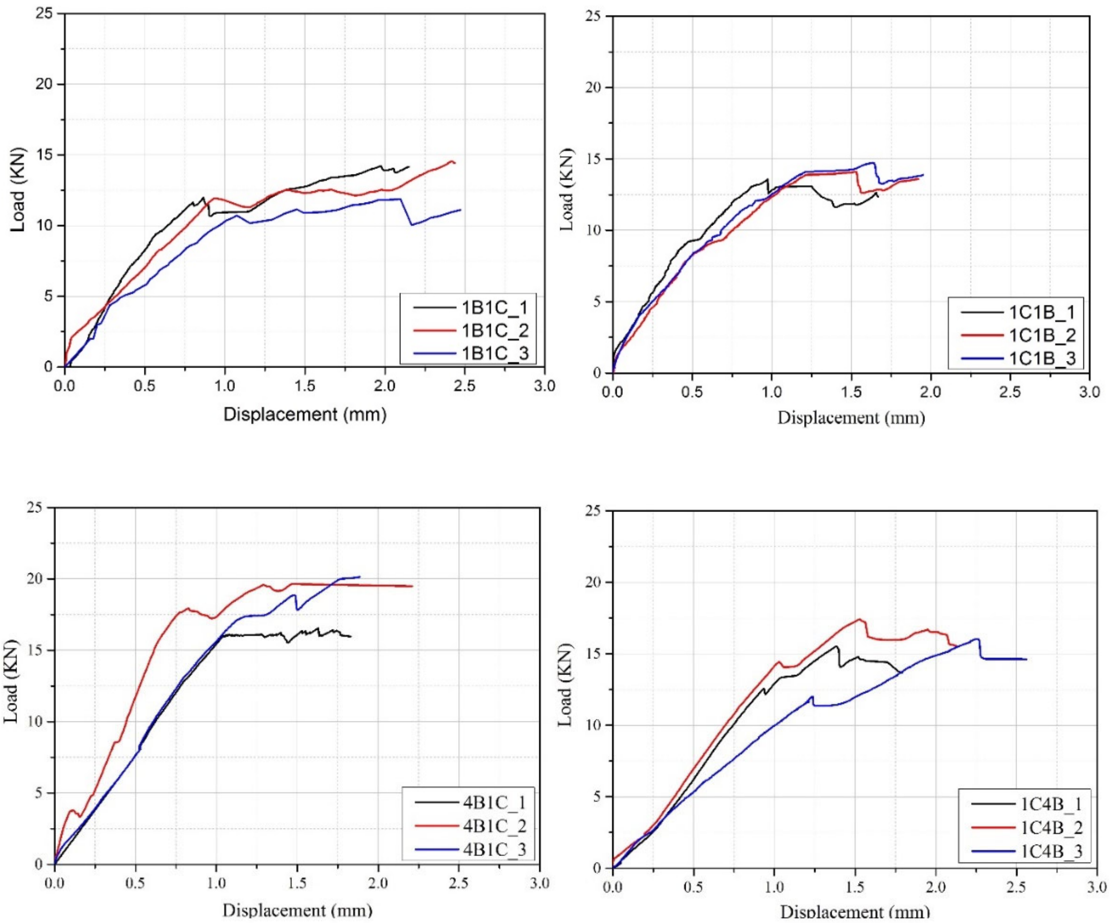

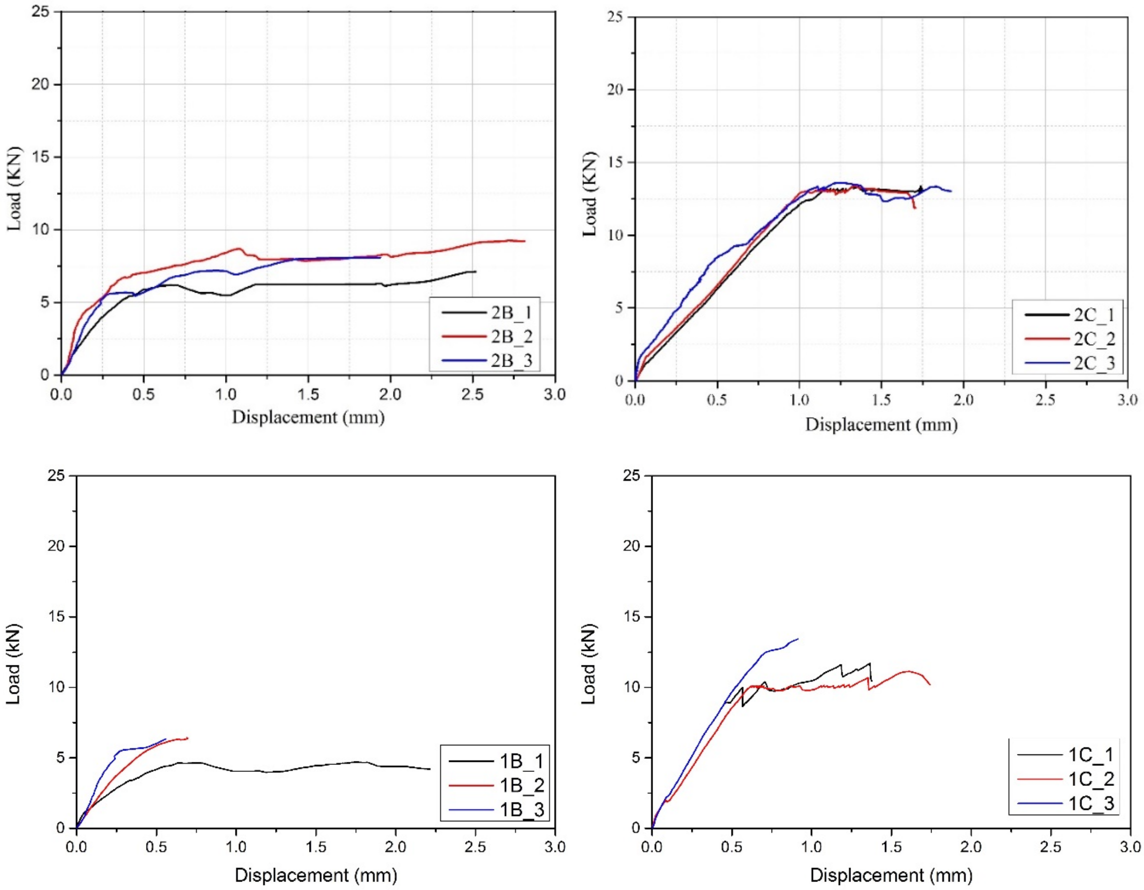

Figure 5. Load-displacement curves

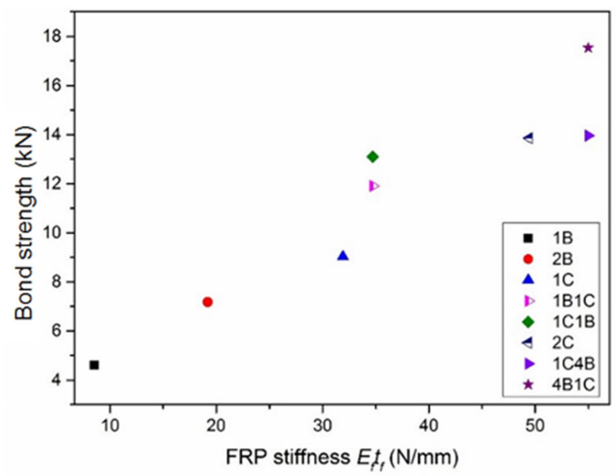

Figure 6. Relationship between FRP stiffness and bonding strength

Figure 7 shows the typical load-displacement curve for the specimen G2_1C1B_2. Theoretically, three stages exist in the load and displacement curves, i.e. elastic stage, softening stage, and debonding stage. After elastic stage, interfacial softening induced by microcracking at adhesive-concrete interface initiates along with the loss of shear stress as the increase of the interfacial shear slip [44]. Debonding initiated at the loaded end when reaching the debonding load shown in red mark, followed by debonding plateau. In this study, all the specimens were prepared with 200 mm bond length, which was longer than the corresponding effective lengths and enough to develop the debonding plateau.

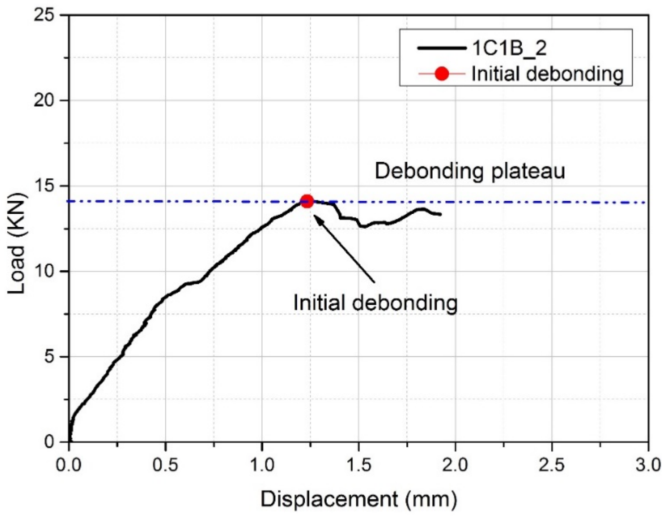

Figure 7. Debonding load and typical load-displacement curve (G2_1C1B_2)

3.3 Strain distribution of hybrid FRPs

DIC images of strain fields (ε) in the anchorage area along the loading direction at different loading levels for the specimen G2_1C1B_2 are shown in Figure 8. When the applied load increased before reaching the debonding load, the FRP strain also increased and redistributed within the anchorage area. It should be noted that the strain can only develop within a certain region, which is called the effective bond length [7, 23, 45, 46]. After reaching the debonding load, the FRP strain redistributed along the anchorage area and propagated toward the free end until the completed debonding of the FRP sheet. The development of strain fields implies the progress of interfacial damage of the FRP-to-concrete interface.

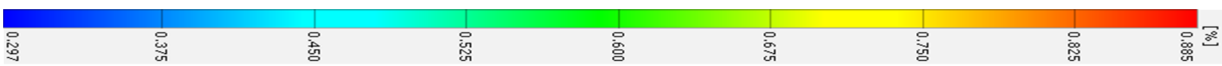

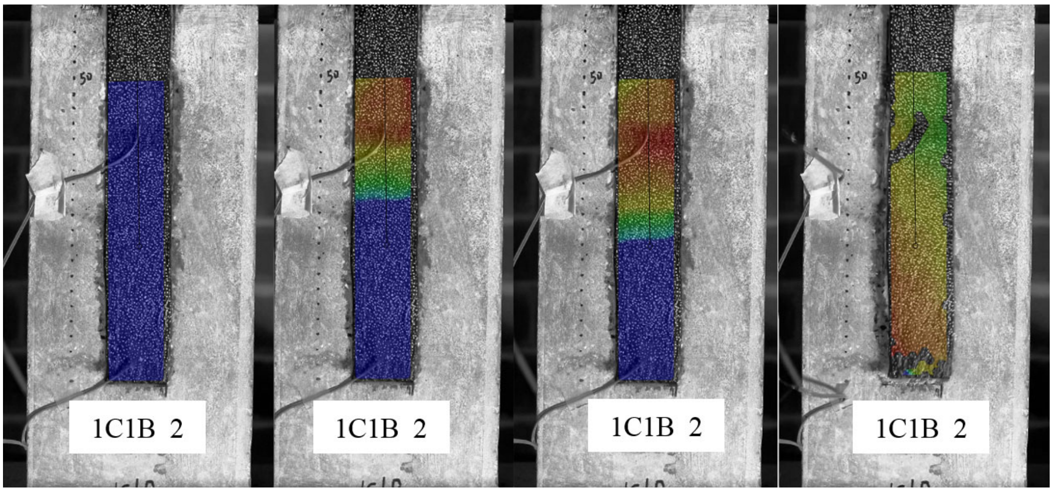

(a) 0 kN; (b) 13.28 kN (Debonding load); (c) 13.64 kN; (d) Completed debonding

Figure 8. Distribution and propagation of FRP strain of G2_1C1B_2 at different loading stages

3.3.1 Smoothen method

The fluctuation of FRP strain was observed, which was caused by the ambient noise during tests and the local material variation in the FRP laminate [47]. To reduce the fluctuation, two methods (i.e. averaging spatial filter method and median spatial filter method) [48] were used in this study. The graphs of the specimens filtered by these two methods are shown in Figure 9 (a). The smoothened strain by the median filtering method is closer to the measured strain traced from strain gauge SG1. Therefore, the median filtering method is used for strain smoothening in this study. Figure 9 (b) shows the comparison between the DIC results and the smoothened results. The distribution of strain exhibits a descending tendency. The local strain fluctuation especially for the DIC strain at 13.28 kN is due to the stress concentration caused by the aggregates embedded between the FRP sheet and concrete block. Curve fitting procedure is conducted to eliminate the fluctuations of strain distribution. In brief, the DIC technique and the filtering method yield reliable strain as verified by the experimental measures from the strain gauge so that they were utilized to monitor the FRP strain and its distribution.

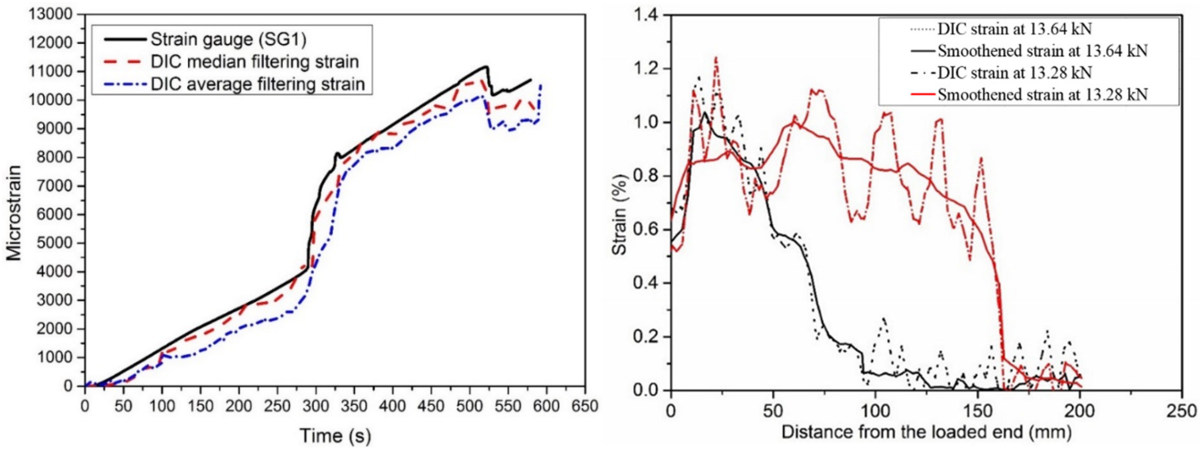

(a) (b)

Figure 9. (a) Strain comparisons by using average filtering and median filtering methods for G2_1C1B_2; (b) Strain distribution of G2_1C1B_2 at different loading levels

3.3.2 Fitting procedure for strain

A non-linear formula expressed by equation (3) [47] is adopted for the fitting procedure. It is found that the expression can simulate the strain distribution along the anchorage length, as follows:

$$\varepsilon(\mathrm{x}) = \mathrm{a} + \frac{b}{1+\exp(\frac{x_o - x}{\beta})^{\mathrm{c}}} \qquad (3)$$

where a, b, c, β and x_o are determined by using non-linear regression analysis of the smoothened strain and x is the distance from the loaded end. Figure 10 shows the strain distribution of specimen G2_1C1B_2 at the debonding load of 13.28 kN. The ultimate strain was approximately 0.9% when debonding load P_d was reached. After reaching the debonding load P_d, the load and strain stopped increasing, which indicated the forming of effective bond length. The effective bond length is the bond length beyond which no further increase in ultimate load can be achieved [7].

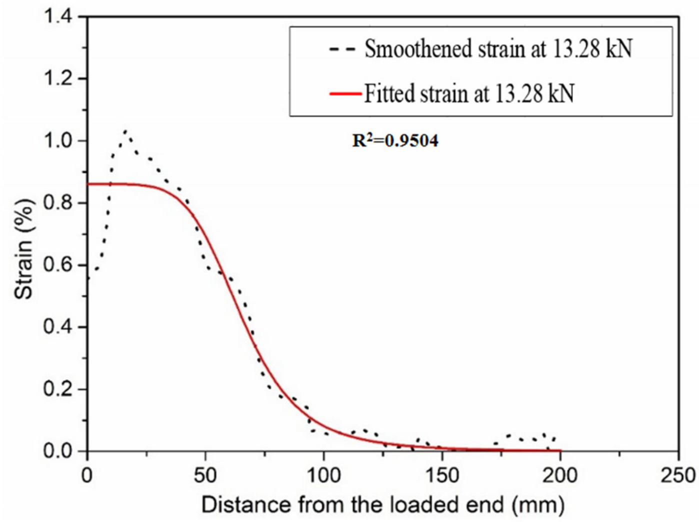

Figure 10. Strain distribution of G2_1C1B_2 at debonding load

3.3.3 Effective bond length

Figure 11 illustrates the strain field of the effective bond length for specimen G2_1C1B_2 at the debonding load of 13.28 kN. The black points at the left edge of the concrete substrate were marked every 10 mm to measure the effective bond length. The total bonded length was 200 mm. The 50 mm un-bonded region is to eliminate the edge effect of the concrete blocks. The effective bond length can be determined by the strain contour. The effective bond length is defined as the bond length over which the strain decreases from the peak value to zero [7]. Therefore, the effective bond length of specimen G2_1C1B_2 was 78 mm at the debonding load of 13.28 KN as can be seen in Figure 11.

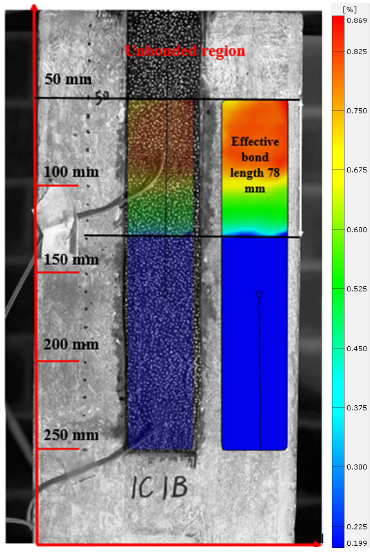

Figure 11. Effective bond length of specimen G2_1C1B_2 at debonding load of 13.28 kN

3.4 Bond stress and local slip calculation

The bond-slip relationship in the longitudinal direction can be obtained from the smoothened strain by equations (4) and (5). The interfacial bond stress distribution within the bonded length can be evaluated by imposing the equilibrium condition of a FRP sheet with a length *dx* as follows:

$$\tau(x) = t_f E_f \frac{\mathrm{d}\varepsilon_\mathrm{f}}{\mathrm{dx}} \quad (4)$$

where $\tau(x)$ is the interfacial bond stress, $\frac{d\varepsilon_\mathrm{f}}{dx}$ is the gradient of FRP strain along the bonded length, t_f is the FRP thickness, and E_f is the FRP elastic modulus. In addition, the local slip $s(x)$ between FRP plate and concrete at distance x from the free end of the specimen can be calculated by assuming a zero slip in the free end as [49]:

$$s(x) = \int_0^\infty \varepsilon_f dx \quad (5)$$

3.4.1 Bond stress distribution

Figure 12 shows the interfacial bond stress for G2_1C1B_2 at 13.28 kN (debonding load) and 13.65 kN based on the smoothened strain profile by equation (3). It can be seen that the plotted graph can well present the development of the interfacial bond stress. The interfacial shear stress initially rises with the applied load. After reaching its peak value, the shear stress starts to decrease until the debonding of FRP sheet is completed. The bond stress obtained from the fitted strain matches well the smoothened result, and the fluctuation of the bond stress can be eliminated by the fitting strain. With the increase in applied load, the peak bond stress propagates from the loaded end along the length of the FRP sheet, which implies the debonding propagation.

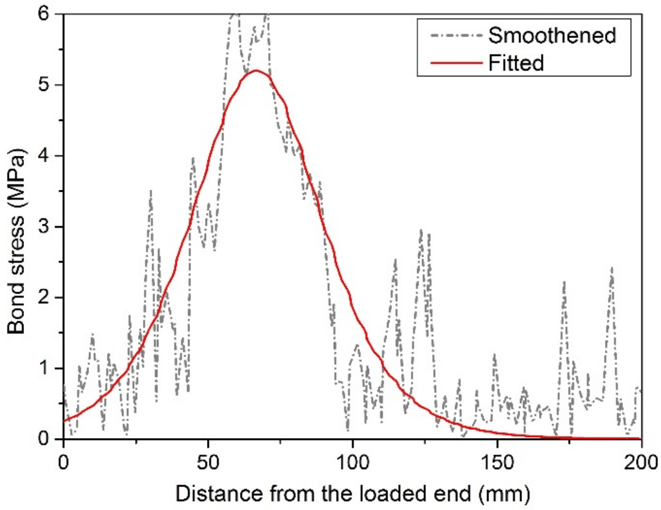

Figure 12. Bond stress distribution along the bonded length of specimen G2_1C1B_2

3.4.2 Local slip distribution

Figure 13 shows the local slip distribution for G2_1C1B_2 at the debonding load of 13.28 kN along the bonded length based on the smoothened strain profile by equation (3). The local slip between FRP plate and concrete shows an increasing trend from the free end during the loading process. After reaching the debonding load, the local slip increases sharply, which indicates the debonding occurrence.

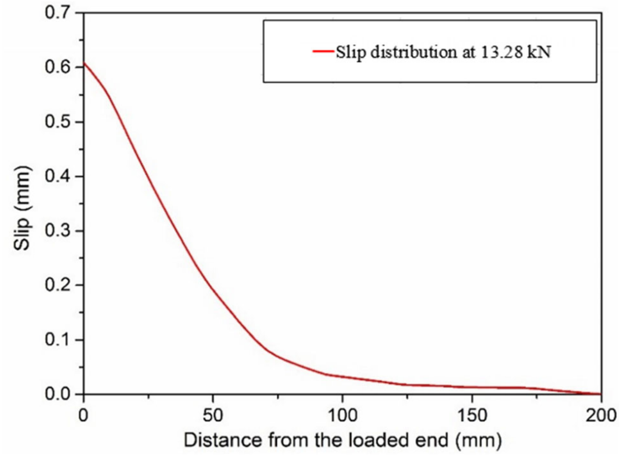

Figure 13. Local slip distribution calculated from smoothened strain at the debonding load of 13.28 kN for G2_1C1B_2

3.4.3 Bond-slip relationship

Figure 14 shows the bond-slip curve of Specimen G2_1C1B_2 at 13.28 kN based on the smoothened strain and the fitted strain profile. The bond-slip curve estimated from the fitted strain is close to the smoothened result. The interfacial shear stress increases sharply with the increasing applied loads, and then drops gradually after reaching the peak shear stress until full debonding. It is obvious that the bond-slip constitutive relation exhibits a softening behavior. It is approximately linear up to 40% of the maximum shear stress, after which it increases nonlinearly up to the peak stress. The results agreed well with those in the previous study [50]. From the experimental results, the maximum bond stress $\tau_{\max}$ and the corresponding slip s_o of the specimen G2_1C1B_2 was 5.11 MPa and 0.099 mm, respectively. After reaching the peak stress, a nonlinear softening behavior is observed due to the slip. Therefore, the non-linear bond-slip curves contain an ascending branch ($0 < s \leq s_o$) and a descending branch ($s > s_o$). The area under the bond-slip curve represents the interfacial fracture energy G_f, defined as:

$$G_f = \int \tau ds \tag{6}$$

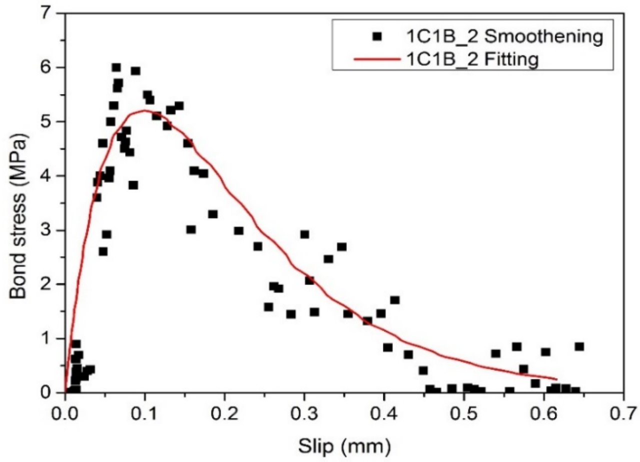

Figure 14. Bond-slip curve for G2_1C1B_2

The fitted results of the maximum bond stress $\tau_{\max}$, slip s_o at the maximum bond stress, and fracture energy G_f are summarized in Table 3.

Table 3. Test results of debonding loads, bond stress, slip, fracture energy and parameter *c*

Specimen	Debonding load (kN)	Fitting parameter (*c*)	Fracture energy G_f (N/mm)	Parameters for the developed model τ_{max} (MPa)	s_o (mm)	s_u (mm)	Failure mode
G1_1B_1	4.61	0.54	0.71	2.36	0.110	0.550	D
G1_1B_2	N/A	N/A	N/A	N/A	N/A	N/A	R
G1_1B_3	N/A	N/A	N/A	N/A	N/A	N/A	R
G1_1C_1	10.04	0.51	0.68	4.53	0.051	0.290	D
G1_1C_2	N/A	N/A	N/A	N/A	N/A	N/A	R
G1_1C_3	8.01	0.50	0.67	5.01	0.049	0.271	D
G2_1B1C_1	12.02	0.55	1.80	6.50	0.089	0.440	D
G2_1B1C_2	11.95	0.54	1.78	6.07	0.087	0.460	D
G2_1B1C_3	11.77	0.56	1.79	5.99	0.078	0.450	D
G2_1C1B_1	12.79	0.51	1.39	5.11	0.099	0.505	D
G2_1C1B_2	13.28	0.55	1.43	5.20	0.093	0.500	D
G2_1C1B_3	13.22	0.52	1.41	5.16	0.089	0.530	D
G2_2B_1	6.51	0.53	0.81	5.77	0.091	0.460	D
G2_2B_2	7.78	0.54	0.72	5.68	0.093	0.440	D

G2_2B_3	7.21	0.53	0.71	5.59	0.096	0.410	D
G2_2C_1	13.87	0.56	0.95	5.21	0.058	0.280	D
G2_2C_2	13.83	0.54	0.99	5.23	0.057	0.310	D
G2_2C_3	13.85	0.52	0.93	5.60	0.049	0.340	D
G3_1C4B_1	15.18	0.52	1.90	5.67	0.119	0.610	D
G3_1C4B_2	14.19	0.50	1.95	5.70	0.110	0.613	D
G3_1C4B_3	12.50	0.55	1.78	6.11	0.114	0.630	D
G3_4B1C _1	17.33	0.54	1.10	6.39	0.064	0.290	D
G3_4B1C _2	17.69	0.55	1.09	6.48	0.061	0.310	D
G3_4B1C _3	17.58	0.50	1.04	7.11	0.059	0.330	D

Note: R - Rupture of FRP sheet. D - Debonding of FRP sheet.

3.4.4 Simplified bond-slip relationship

The bond-slip model is important for analysing the behaviour of FRP-strengthened concrete structures because it describes the relationship between the local interfacial shear stress and the local slip [51]. To describe the interfacial bond properties, the shape of the bond-slip model should be chosen firstly. The CEB-FIP model (CIB 1993) [52] is used to simplify the bond-slip relationship due to its simplicity and good match with the experimental results. The bond-slip relationship is determined by four parameters, i.e. the maximum shear stress $\tau_{\max}$, the slip s_o at the maximum shear stress, the ultimate slip s_u, and *c*, which is the fitting parameter from the experimental data. Four key parameters extracted from the non-linear bond-slip curves are listed in Table 3. It can be seen that the bond-slip curves cover an ascending branch and a descending branch as shown in Figure 15. The nonlinear ascending part can be expressed as a hyperbolic equation. The descending branch can be depicted by a linear equation. The bond-slip relationship is proposed by using the following formulae:

$$\tau(s) = \tau_{max}\left(\frac{s}{s_o}\right)^c,\ 0 \le s \le s_o \tag{7}$$

$$\tau(s) = \tau_{\max}\frac{s_u - s}{s_u - s_o},\ 0 \le s \le s_o \tag{8}$$

$$\tau(s) = 0,\ s_u \le s \tag{9}$$

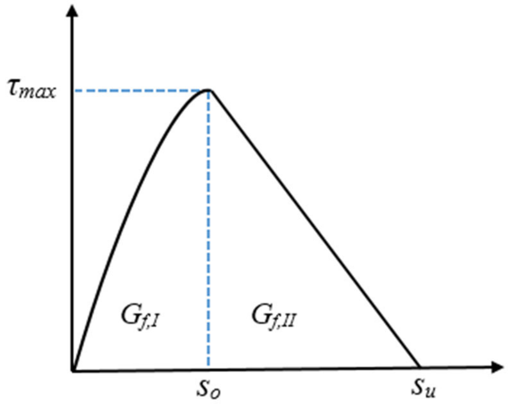

Figure 15. Typical bond-slip relationship

For all the specimens, the nonlinear descending branch can be converted into a linear part in order to compare with the current bilinear bond-slip models. The conversion process always maintain the same interfacial fracture energy for the curves before and after converting. The interfacial fracture energy is used to determine the ultimate slip s_u. For the simplified bond-slip, the interfacial fracture energy $G_{f,s}$ can be obtained by integrating the bond stress with respect to the slip:

$$G_{f,s} = G_{f,I} + G_{f,\mathrm{II}} = \int_0^{S_O} \tau_{\max}\left(\frac{s}{s_o}\right)^c ds + \frac{1}{2}\tau_{\max}\left(s_u - s_o\right) \tag{10}$$

For the non-linear bond-slip, $G_{f,I}$ and $G_{f,II}$ can be obtained by integrating the bond stress with respect to the slip to figure out the interfacial fracture energy $G_{f,n}$, as shown in equation

(11). The key parameters c and ultimate slip s_u can be obtained for all the specimens and are listed in Table 3.

$$G_{f,n} = G_{f,I} + G_{f,\mathrm{II}} = \int_0^{s_o} \tau(s)\,ds + \int_{s_o}^{\infty} \tau(s)\,ds \quad (11)$$

3.5 Effect of FRP stacking order

3.5.1 Debonding load

The debonding loads (P_d) of the tested specimens are given in Table 4. As can be seen that the debonding loads of two specimens with the same combination but different stacking order were significantly different. For example, the debonding load of G2_1B1C (i.e. P_d=11.91 kN) is lower than that of G2_1C1B (i.e. P_d=13.09 kN). These specimens were made of the same type and number of FRP layers but they were bonded to the concrete blocks by different sequences. These experimental results have shown that the stiffness and thickness of the first layer of the hybrid FRP sheets affected the bonding behaviour. Although both hybrid FRPs (i.e. G2_1B1C and G2_1C1B) have the same stiffness ($E_f t_f$), the higher debonding strength was observed when the CFRP layer (i.e. G1_1C1B) is attached to the concrete block. For specimens G2_1C1C and G3_4B1C, four layers of BFRP sheets have the thickness of 0.48 mm, which is much thicker than that of one layer of CFRP sheet (i.e. 0.167 mm). When one layer of CFRP was attached to the concrete, the lower debonding load was achieved as the specimen G2_1C1C experienced lower debonding load (P_d=13.85 kN) than the specimen G3_4B1C (P_d=17.54 kN). It was observed that for the similar stiffness of the contacting layer of FRP, the higher debonding strength can be achieved when the thicker FRP sheets (G3_4B1C) are attached to the concrete. This is because the thicker FRP resulted in higher interfacial fracture energy (G_f). As shown in Figure 16, the average value of fracture energy of the specimen G2_1C1C and G3_4B1C is 0.96 and 1.08 N/mm, respectively. The bond strength is proportional to the fracture energy [43, 53]. It is noted that the stiffness of the contacting layer of 1C is approximately similar to that of 4B.

Table 4. Effect of FRP stacking order on the debonding load and the effective bond length

Specimen	G1_1B	G1_1C	G2_1B1C	G2_1C1B	G3_4B1C	G2_1C1C	G3_1C4B
Average debonding load (kN)	4.61	9.00	11.91	13.09	17.54	13.85	14.00
Average effective bond length (mm)	31	59	67	78	81	90	92

Note: The data is averaged from three specimens

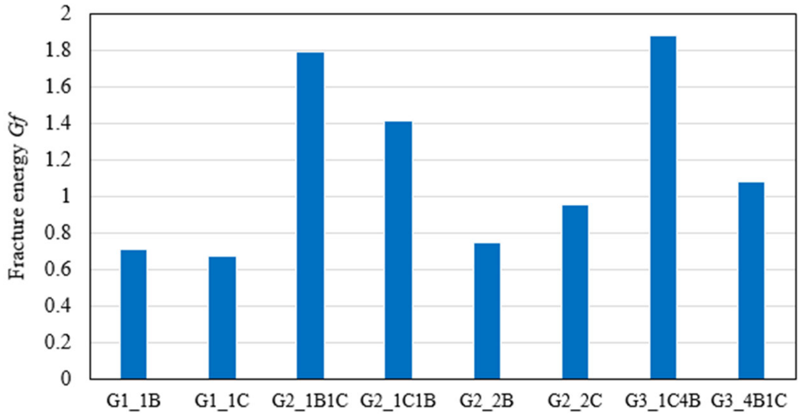

Figure 16. Averaged interfacial fracture energy

3.5.2 Effective bond length

Table 4 also shows the effect of FRP stacking order on the effective bond length. It was observed that the first layer of FRP attached to concrete surface had a great influence on the effective bond length. When one ply of CFRP sheet is attached to the concrete surface prior to one ply of BFRP sheet, a larger effective bond length can be achieved, which means that a larger area of stress distribution can be obtained. There is 14.10% difference caused by the stacking order effect as the effective bond length for G2_1C1B and G2_1B1C is 78 mm and 67 mm, respectively. Theoretically, the effective bond length of G3_1C4B and G3_4B1C should be the same due to the similar stiffness (i.e. the stiffness of 1C4B is similar to that of 4B1C) according to the previous effective bond length models [2, 46]. This is because the effective bond length is proportional to the FRP stiffness ($E_f t_f$), and a stiffer FRP sheet can achieve a longer effective bond length, which is consistent with the literature [25]. However, the effective bond length of G3_1C4B is 92 mm which is larger than that of G3_4B1C (i.e. L_e = 81 mm). The 11.96% difference should be caused by the FRP stacking order and the relative slips within the internal layers between FRP sheets and the contacting layer between FRP and concrete, as shown in Figure 17. It should be noted that multilayer BFRP sheets have been bonded together to increase the hybrid stiffness (i.e. 4B). The shear redistribution induces the variations in effective bond length. The shear redistribution in multilayered FRPs has also been specified in the literature [44].

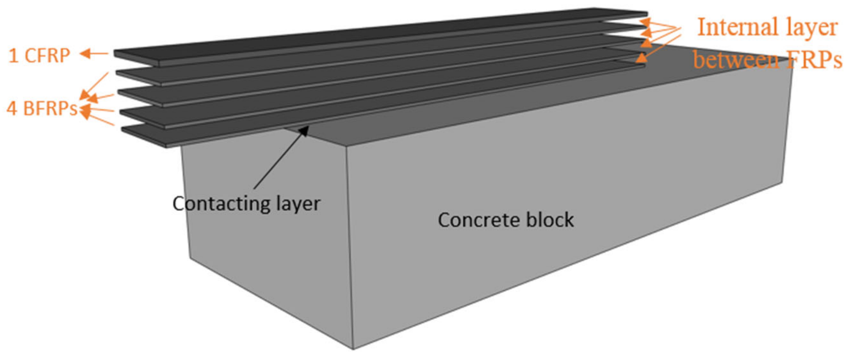

Figure 17. Internal layers between FRPs and contacting layer of FRP-concrete

3.5.3 Bond stress and local slip

For specimens G2_1C1B_2 and G2_1B1C_2, the bond-slip relationships are shown in Figure 18 (a). It can be seen that FRP stacking order had a significant influence on the bond-slip relationship. The maximum bond stress (τ_{max}) for G2_1B1C_2 is 6.07 MPa and G2_1C1B_2 is 5.20 MPa which meant that the peak bond stress was reduced when the stiffer FRP plate was used as the contacting layer. The peak bond stresses of these two cases varied by 16.73%. However, the ultimate slip improved when a stiffer FRP sheet was used. The fracture energy (G_f) for specimens G2_1B1C_2B and G2_1C1B_2 were 1.78 N/mm and 1.43 N/mm, respectively, which meant the specimen G2_1B1C_2B had a greater ability to absorb energy.

Both the specimens G2_1C4B_2 and G2_4B1C_2 consisted of 1C and 4B, which had the similar stiffness. However, the maximum shear stress and slip values were quite different as there was a 13.68% difference in the peak bond stress and 49.43% in the ultimate slip, as shown in Figure 18 (b). When the contacting layer was CFRP sheet (1C), the maximum shear stress was lower than that of BFRP sheets (4B), which meant that the interfacial shear stress was reduced if the stiffer FRP plate was placed as a contacting layer. However, the ultimate slip could be greatly improved when the CFRP was placed as a contacting layer as compared to BFRP. Specimen G2_1C4B_2 possessed a higher capacity for energy absorption than that of Specimen G2_4B1C_2 as there was a 44.10% difference in the test results of fracture energy, as given in Table 3. Compared with the sole FRP strengthened concrete, the strain distribution is more complicated as the shear stress redistribution occurred in the internal layers between FRP, which can be evidenced by Figure 19. This is caused by the different strain capacity of FRP composite. The full-fields strain was obtained from the surface rather than the internal layers. The obtained shear stress and slip was calculated based on the surface strain in this study. This should be a possible reason that the obtained shear stress and slip are quite different from each other (i.e. 1C1B and 1B1C or 1C4B and 4B1C).

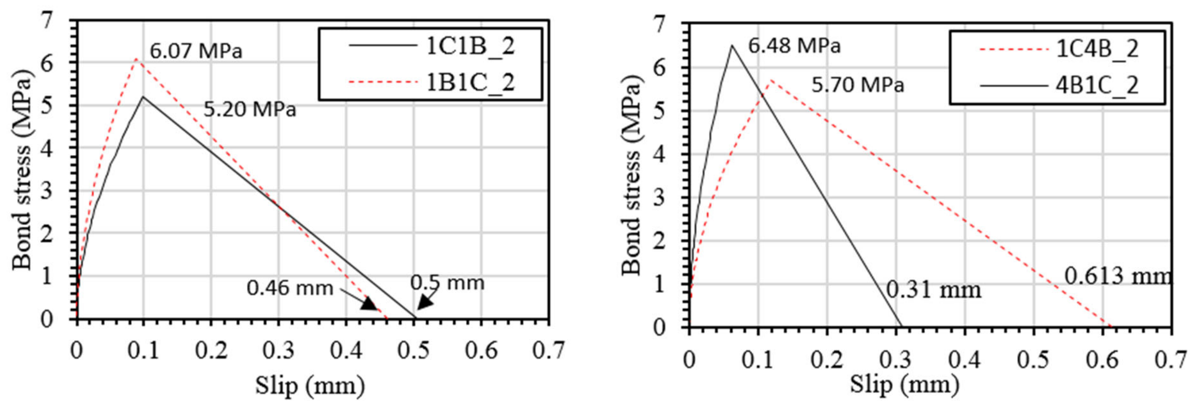

(a) (b)

Figure 18. Bond-slip curves for (a) hybrid FRPs (G2_1C1B_2 and G2_1B1C_2); (b) hybrid FRPs with four-ply of BFRP and one ply of CFRP (G3_1C4B_2 and G3_4B1C_2)

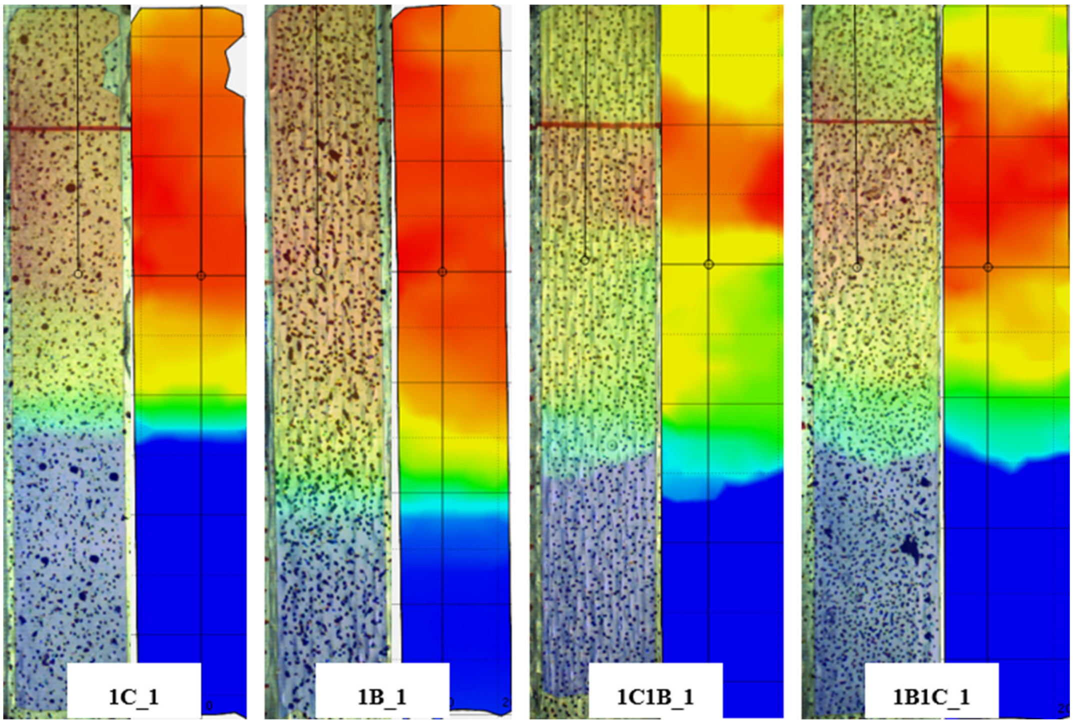

Figure 19. Strain contours

4. Comparison of experimental results with theoretical predictions

4.1 Bond strength model

Two bond strength models i.e. Lu et al. [43] and Chen and Teng [2] were adopted for the bond strength prediction of single type of FRP sheet. Table 5 lists the experimental and predicted debonding loads for all the specimens. Among the specimens of group 1B, one specimen experienced debonding and the other two ruptured. Among the specimens of group 1C, two specimens experienced debonding and the other one ruptured. For the specimens 1B and 1C, the bonding strength is close to the tensile strength of FRP, which leads to either debonding failure or FRP rupture. The rest of the specimens experienced debonding failure. As given in Table 5, the bond strength of hybrid FRPs cannot be well predicted by the models by Lu et al. [43] and Chen and Teng [2]. These two models predict the same debonding loads for the specimens G2_1C1B and G2_1B1C or G3_1C4B and G3_4B1C, respectively. However, the experimental results show different results, e.g. 11.91 kN for G2_1B1C and 13.09 kN for G2_1C1B even though these specimens had the same stiffness.

The significant variation between the predicted versus the experimental results may be resulted from the difference in the stiffness of the contacting layer. When using equation (2) to predict the stiffness, it causes a variation of 9.7% and 14.1% for 1B1C/1C1B and 1C4B/4B1C as compared to the measured stiffness, respectively, as given in Table 2. Therefore, the test result of elastic modulus rather than the predicted elastic modulus should yield better prediction of the debonding load. Figure 20 shows the errors of the predicted effective bond length and there are considerable differences between the experimental and analytical results, especially for the hybrid specimens. It should be noted that the stiffness used in calculations was the measured results.

Chen and Teng [2] bond strength model is given as:

$$P_u = 0.427\beta_1\beta_w b_f L_e\sqrt{f_{co}} \tag{12}$$

where $\beta_1 = \begin{cases} 1, & L \geq L_e \\ \sin\dfrac{\pi L}{2L_e}, & L < L_e \end{cases}$, $\beta_w = \sqrt{\dfrac{2 - b_f / b_c}{1 + b_f / b_c}}$, and $L_e = \sqrt{\dfrac{E_f t_f}{\sqrt{f_{co}}}}$.

Lu et al. [43] bond strength model is given by:

$$P_u = b_p\beta_1\sqrt{2E_f t_f G_f} \tag{13}$$

where $\beta_1 = \begin{cases} 1, & L \geq L_e \\ \left(2 - \dfrac{L}{L_e}\right)\dfrac{L}{L_e}, & L < L_e \end{cases}$, $\beta_w = \sqrt{\dfrac{2.25 - b_f / b_c}{1.25 + b_f / b_c}}$, and $G_f = 0.308\beta_w^{\ 2}\sqrt{f_t}$

Table 5. Experimental and predicted debonding loads

Specimen	$P_{u,exp}$ (kN)	Lu et al. Model [43]		Chen and Teng model [2]	
		$P_{u,pre}$ (kN)	$P_{u,pre}/P_{u,exp}$	$P_{u,pre}$ (kN)	$P_{u,pre}/P_{u,exp}$
Sole FRP					
G1_1B	4.61	4.80	1.04	5.68	1.23
G1_1C	9.00	8.37	0.93	9.91	1.10
G2_2B	7.17	6.88	0.96	8.15	1.13
G2_2C	13.85	11.83	0.85	14.02	1.01

Mean value			0.95		1.12
		Hybrid FRP			
G2_1B1C	11.91	9.25	0.77	10.96	0.92
G2_1C1B	13.09	9.25	0.71	10.96	0.83
G3_1C4B	14.00	11.65	0.83	13.79	0.98
G3_4B1C	17.54	11.65	0.66	13.79	0.79
Mean value			0.74		0.88

Note: The data is averaged from three specimens

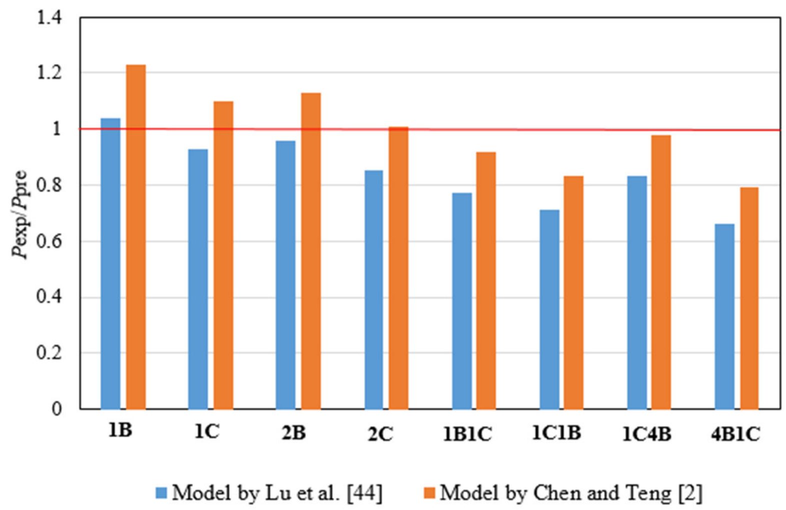

Figure 20. Comparisons of the predicted debonding loads with the test results

4.2 Effective bond length model

Table 6 lists the experimental and predicted effective bond length L_e for all the specimens. Two effective bond length models by Chen and Teng [2] and Lu [54] are employed to make comparisons. The errors of the predicted effective bond length for hybrid FRPs are given in Figure 21. These two models can give accurate predictions for single type of FRP sheet with low variations. However, the effective bond length of hybrid FRP sheets, i.e. specimen 1C1B and 4B1C, cannot be well predicted due to the effects of FRP stacking order.

Chen and Teng [2] effective bond length model is given as:

$$L_e = \sqrt{\frac{E_f t_f}{\sqrt{f_{co}}}} \tag{14}$$

where $E_f t_f$ is the stiffness of FRP, and f_{co} is the concrete compressive strength.

Lu [54] effective bond length model is given as:

$$L_e = 1.33 \frac{\sqrt{E_f t_f}}{f_t} \tag{15}$$

where $E_f t_f$ is the stiffness of FRP, and f_t is the concrete tensile strength.

Table 6. Experimental and predicted results of the effective bond length L_e

Specimen	***Le*,exp (mm)**	**Lu model [54]**		**Chen and Teng model [2]**	
		$L_{e,pre}$ (mm)	$L_{e,pre}/L_{e,exp}$	$L_{e,pre}$ (mm)	$L_{e,pre}/L_{e,exp}$
Sole FRP					
G1_1B	31	36.78	1.19	36.65	1.18
G1_1C	59	68.89	1.17	68.64	1.16
G2_2B	60	52.01	0.87	51.83	0.86
G2_2C	90	97.42	1.08	97.07	1.08
Mean value			1.08		1.07
Hybrid FRP					
G2_1B1C	67	78.10	1.17	77.81	1.16
G2_1C1B	78	78.10	1.00	77.81	1.00
G3_1C4B	92	100.78	1.10	100.42	1.09
G3_4B1C	81	100.78	1.24	100.42	1.24
Mean value			1.13		1.12

Note: The data is averaged from three specimens

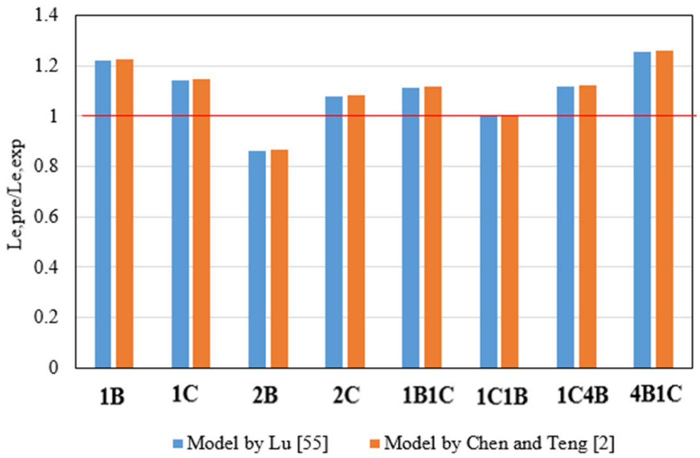

Figure 21. Comparisons of the predicted and tested effective bond length

4.3 Bond-slip model

Two bond-slip models by Lu et al. [43] and Sun et al. [44] are employed and their predictions are compared to the experimental results. Lu et al. [43] proposed a bilinear model based on the experimental results in the literature. The maximum interfacial shear stress $\tau_{\max}$, the elastic slip s_o, the interfacial fracture energy G_f and the ultimate slip s_u are given as:

$$\tau(s) = \tau_{max}(\frac{s}{s_o}),\ 0 \le s \le s_o \tag{16}$$

$$\tau(s) = \tau_{max}(\frac{s_o - s}{s_u - s_o}),\ s_o \le s \le s_u \tag{17}$$

where $\tau_{max} = 1.5\beta_w f_t$, $s_o = 0.0195\beta_w f_t$, $s_u = \dfrac{2G_f}{\tau_{max}}$, $G_f = 0.308\beta_w{}^2\sqrt{f_t}$, $\alpha = \dfrac{1}{\dfrac{G_f}{\tau_{max}s_o} - \dfrac{2}{3}}$,

$\beta_w = \sqrt{\dfrac{2.25 - b_f / b_c}{1.25 + b_f / b_c}}$, and b_f and b_c are the width of FRP and concrete blocks, respectively.

Another bilinear bond-slip model was proposed by Sun et al. [44]. The expressions of the bilinear model are the same as Lu et al. model [47], as shown in equation (16) and (17). The maximum interfacial shear stress $\tau_{\max}$, the elastic slip s_o, the ultimate slip s_u are given as:

$$\tau_{max} = 1.35 + 0.25\beta_w f_t + 0.62 f_t,$$

$$s_o = 0.016 - 0.0046\beta_w f_t + 0.11\beta_w,$$

$$s_u = -0.06 + \left(0.88 - 0.23\,\beta_w{}^2\right) f_t^{-0.5}\beta_w{}^{0.5},$$

$$\beta_w = \sqrt{\frac{1.9 - b_f / b_c}{0.9 + b_f / b_c}},$$

where b_f and b_c are the width ratio of FRP and concrete block, respectively.

Figure 22 (a-e) shows the predicted and experimental results. It can be seen that Sun et al. [44] model underestimates the maximum shear stress not only for sole type of FRP (1C and 2C) but also for hybrid FRPs. For the model proposed by Lu et al. [43], the predicted interfacial shear stresses are higher than the testing results of the specimens G2_1C1B and G3_1C4B but lower than those of the specimens G3_4B1C and G2_1B1C.

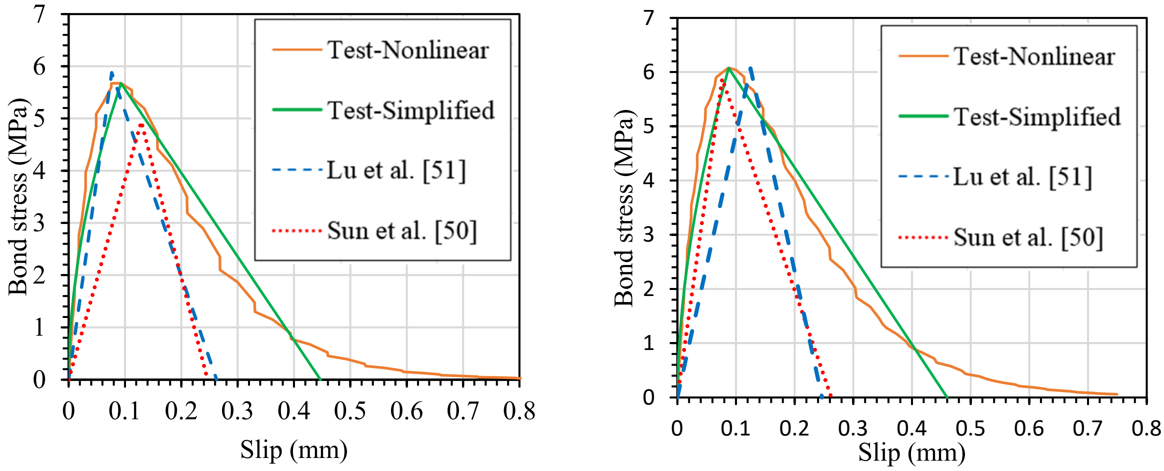

(a) G1_2B_2 (b) G2_1B1C_2

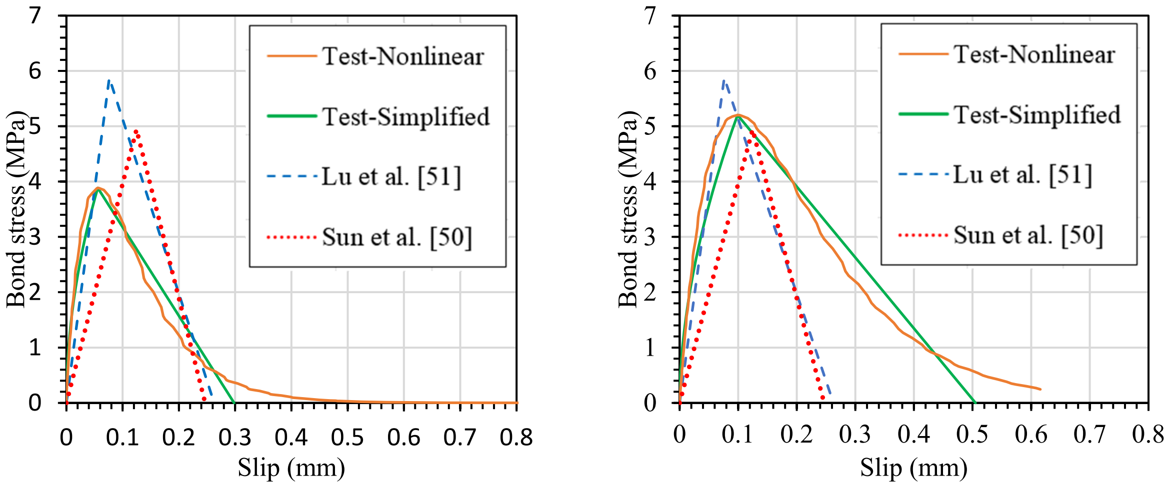

(c) G1_1C_1 (d) G2_1C1B_2

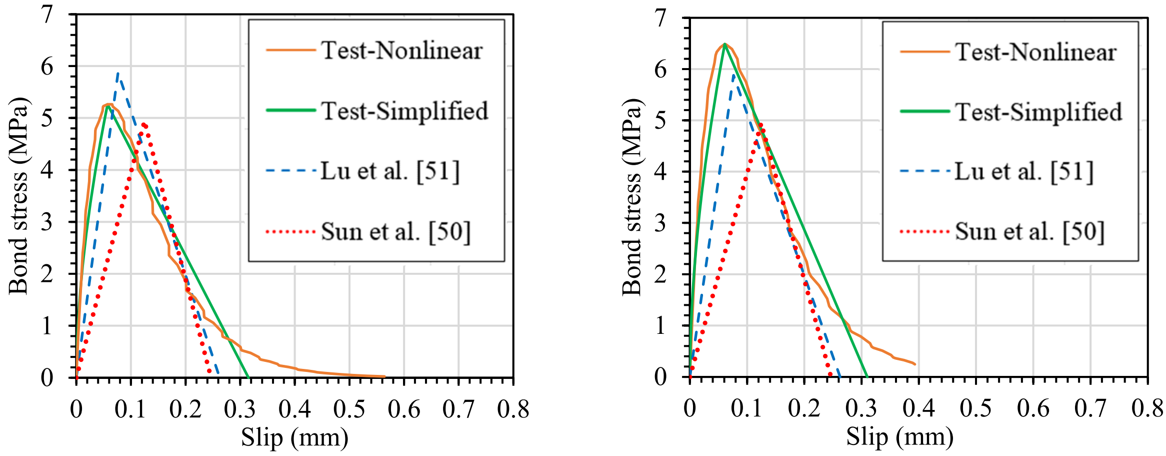

(e) G2_2C_2 (f) G2_4B1C_2

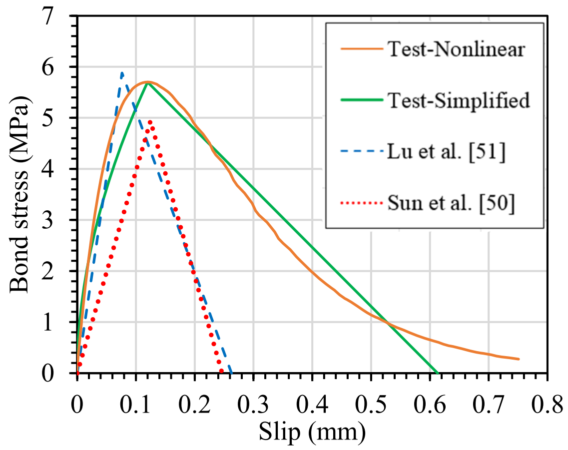

(g) G2_1C4B_2

Figure 22. Comparisons of the predicted and experimental bond-slip curves

5. Proposed model for hybrid FRPs

As can be seen from the discussions above, the existing models cannot predict well the bond behaviour of hybrid FRPs. The primary reason is due to the actual stiffness of hybrid FRP sheets in which the current models could not well predict. This study, thus, proposes new models based on the existing ones and considers the actual stiffness of hybrid FRPs.

5.1 Elastic modulus of hybrid FRPs

The experimental elastic modulus of hybrid FRPs was determined from flat coupon tests. The predicted values are higher than the experimental results, which can be found from Table 7.

Based on the rule of mixtures [37], the tensile stress of hybrid FRPs (f_{HF}) can be determined by the following formula:

$$f_{HF} = [E_C \frac{A_C}{A_{HF}} + E_B \frac{A_B}{A_{HF}}]\varepsilon_{HF}, \ \varepsilon_{HF} \leq \varepsilon_C \quad (18)$$

As FRP is a heterogeneous material and hybrid FRPs consist of multilayered FRP sheets prepared manually by wet lay-up process, the fibres tend to be twisted and poor alignment of the fibres can lead to the reduction in modulus. Therefore, two reduction factors i.e. α and β are introduced to model the modulus reductions. The elastic modulus of hybrid FRPs (E_H) can be expressed as:

$$E_H = \frac{f_{HF}}{\varepsilon_{HF}} = \alpha[\frac{E_C t_C + E_B t_B}{t_C + t_B}] = \frac{f_{HF}}{\beta \varepsilon_C} \quad (19)$$

where E_H is the elastic modulus of hybrid FRPs, E_C and E_B are the elastic modulus of CFRP and BFRP, respectively, f_{HF} is the tensile stress of hybrid FRPs, ε_{HF} is the first rupture strain of hybrid FRPs, ε_C is the rupture strain of one layer of CFRP sheet, α is the reduction factor induced by workmanship, β is the reduction factor caused by the increase of rupture strain in hybrid FRPs, and t_C and t_B are the thickness of CFRP and BFRP layers, respectively. After regression analysis, the reduction factors α = 0.853 and β = 0.742 are determined. As given in Table 7, the elastic modulus of hybrid FRPs is predicted with the mean values of 1.004 (the standard variation SD=0.020) and 1.014 (SD=0.059) by using the equation (19) with the factor α and β, respectively. The equation with the reduction factor α yields more accurate result with higher correlation coefficient ($R^2 = 0.9875$), as shown in Figure 23.

Table 7. Comparisons between experimental and predicted elastic modulus

Hybrid FRPs	$E_{,exp}$ (GPa)	Tensile stress f (MPa)	Rupture strain ε (mm/mm)	$\frac{f_{HF}}{\varepsilon_C}$	$\frac{f_{HF}}{\varepsilon_{HF}}$	$\frac{E_C t_C + E_B t_B}{t_C + t_B}$	Prediction using α	$\frac{E_{,pre}}{E_{,exp}}$	Prediction using β	$\frac{E_{,pre}}{E_{,exp}}$
1C_1	188	1994	0.0106	N/A	N/A	N/A	N/A	N/A	N/A	N/A
1C_2	191	1990	0.0104	N/A	N/A	N/A	N/A	N/A	N/A	N/A
1C_3	193	1986	0.0103	N/A	N/A	N/A	N/A	N/A	N/A	N/A
1C1B_1	124	1649	0.0133	156	124	141	120	0.970	116	0.934
1C1B_2	121	1644	0.0136	158	121	141	120	0.994	117	0.970
1C1B_3	119	1639	0.0138	159	119	141	120	1.011	118	0.992
1C4B_1	87	1281	0.0148	121	87	102	87	1.000	90	1.033
1C4B_2	85	1277	0.0150	123	85	102	87	1.024	91	1.075
1C4B_3	85	1273	0.0149	124	85	102	87	1.024	92	1.083
Average								1.004		1.014
SD								0.020		0.059

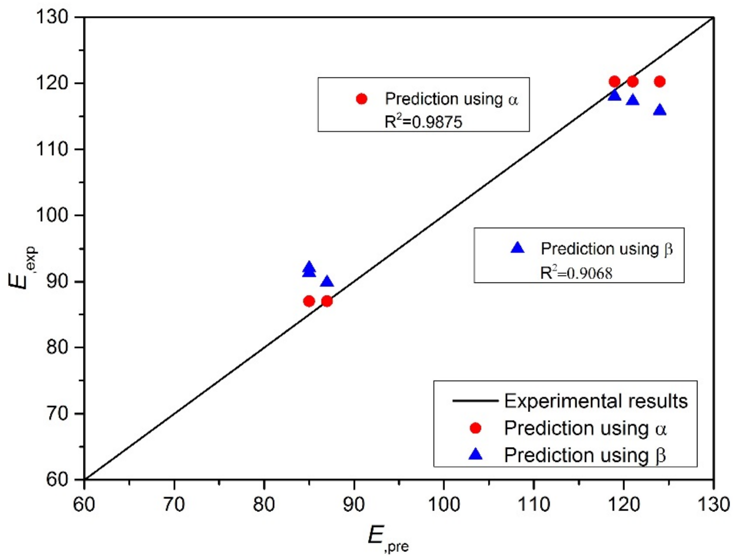

Figure 23. Experimental versus predicted elastic modulus of hybrid FRPs

5.2 Bond strength model for hybrid FRPs

As previously presented, the previous models by Lu et al. [43] and Chen and Teng [2] cannot provide accurate predictions of bond strength for hybrid FRPs. Their capability to predict debonding loads was plotted in Figure 24. It should be noted that the points (i.e. blue and red) which are located above the baseline ($y = x$) represent conservative predictions. Therefore, a more accurate bond strength model for hybrid FRPs should be proposed as bond strength is an important factor controlling debonding failures in FRP-strengthened members [40].

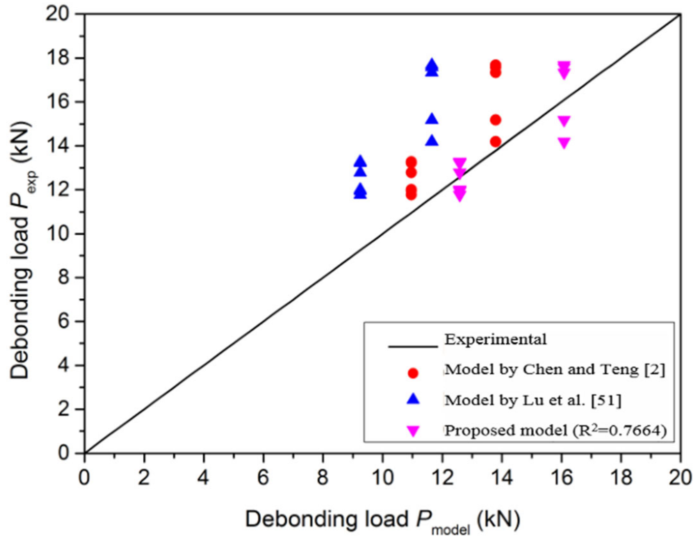

Figure 24. Experimental versus calculated debonding loads for hybrid FRPs

Model by Chen and Teng [2] was used as the basis in modifying the model for hybrid FRP sheets in this study as it was proposed based on effective bond length and gave relatively better predictions. The effective bond length of hybrid FRPs can be predicted by Chen and Teng [2] with a high accuracy (i.e. mean value is 1.11). One calibration factor α was proposed in their bond strength model and α = 0.427 suggested by Yao et al. [40] using 72 single shear specimens. However, this model underestimates the debonding loads of the hybrid FRP in this study. Consequently, the calibration factor α = 0.576 is introduced to equation (12) to better predict the debonding loads, as given in equation (20). It should be noted that the specimen G3_1C4B_3 was not considered in the analysis as well as in the calibration process because a malfunction happened during testing, leading to unreliable results. Figure 25 gives the errors of the debonding loads predicted by the proposed bond strength model. The proposed bond strength model provides more accurate predictions with a mean value of 1.0001 and standard variation 0.075 for the ratio of the tested and predicted bonding strengths. The mean values and the corresponding standard variations of the models by Lu et al. [43] and Chen and Teng [2] are 0.73 and 0.056, and 0.86 and 0.066, respectively.

$$P_u = 0.576\beta_l \beta_w b_f L_e \sqrt{f_{co}} \quad (20)$$

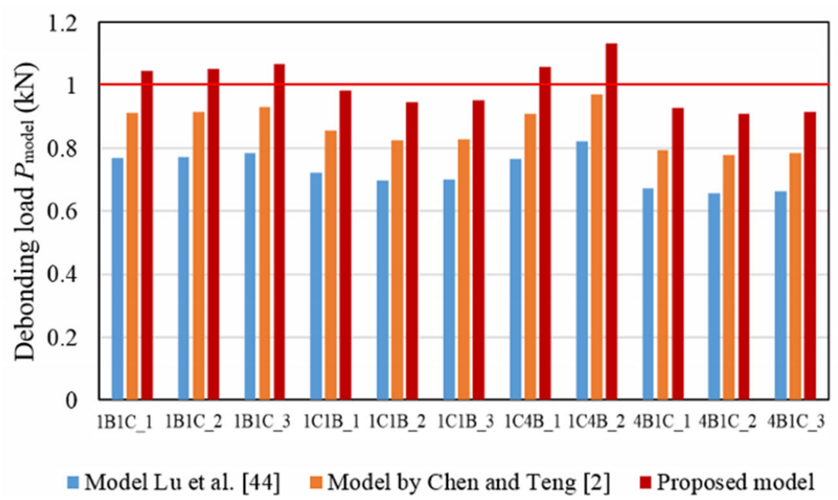

Figure 25. The errors of the predicted debonding loads

5.3 Bond stress model for hybrid FRPs

Based on the comparisons between the predicted and experimental results, the models proposed by Lu et al. [43] and Sun et al. [44] cannot well predict the interfacial shear stress for hybrid FRPs as the predicted bond stresses are constant values for different hybrid specimens, which are different from the experimental results. The parameters β_w and f_t were considered in their models. The experimental results, however, show that the stiffness $E_f t_f$ of FRP should be a key parameter governing the interfacial bond stress, especially for hybrid FRPs. Pellegrino et al. [41] considered the term $\left(n_f E_f t_f\right)^{0.32}$ in their model. Consequently, the interfacial shear stress can be described by the function of $\left(E_f t_f\right)^{0.32}$ [41] and $\beta_w f_t$ [43]. Based on the test results, this study proposes the calibration factor $\alpha = 0.395$ in equation (21) to be used for hybrid FRP. Figure 26 shows the errors of the predicted bond stress. As shown the proposed model provides more accurate results than other models due to its mean value of 1.0001 and standard variation 0.093. The mean values and the corresponding standard variations of the models by Lu et al. [43] and Sun et al. [44] are 1.153, 0.101 and 0.848, 0. 074, respectively.

$$\tau_m = \alpha \left(E_f t_f \right)^{0.32} \beta_w f_t \tag{21}$$

where τ_m is the peak interfacial shear stress, $E_f t_f$ is the stiffness of FRP, β_w is the width ratio of FRP-concrete, and f_t is the tensile strength of concrete.

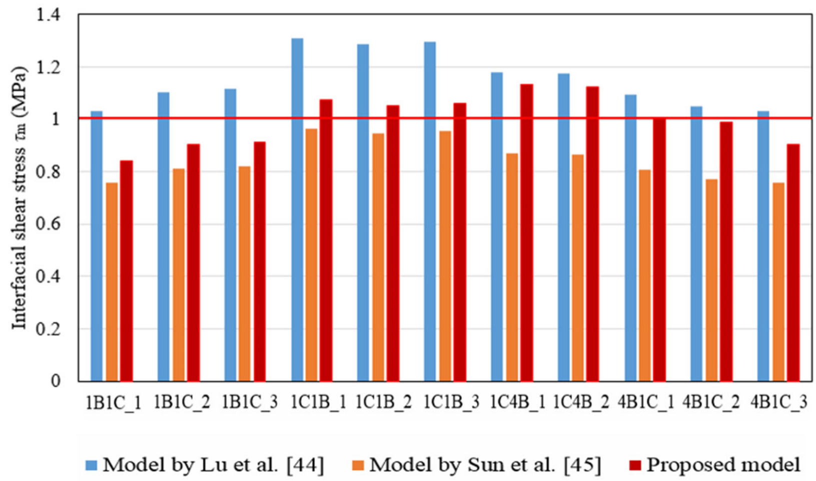

Figure 26. The errors of the predicted interfacial shear stress

6. Conclusion

This study investigates the bond behavior between hybrid FRPs and concrete. The 2D-DIC technique was employed to monitor the fields of displacement and strain. A fitting process was used to obtain bond-slip curves from the fields of strain distributions. Based on the experimental results, the following conclusions can be drawn:

1. The debonding mode of hybrid FRPs is similar to that of sole type of FRP sheets in the single-lap shear tests.

2. The stacking order of hybrid FRPs influences the debonding strength, and the higher debonding strengths can be achieved when a layer of CFRP is attached to the concrete prior to a BFRP layer.
3. FRP stacking order affects the effective bond length because the contacting layer of FRP sheets affects the development of effective bond length. A stiffer FRP sheet can be used as the contacting layer to obtain a longer effective bond length.
4. FRP stacking order has significant effects on the bond-slip relationship. The maximum shear stress reduces if the contacting layer is stuck with a stiffer FRP plate. However, the ultimate slip improves when a stiffer FRP sheet is used.
5. Current bond-slip models in the literature do not well predict the debonding loads and interfacial shear stress for hybrid FRPs. The proposed models in this study based on experimental test results give better predictions of the bond strength and the interfacial shear stress between hybrid FRP sheets and concrete.

The experimental results from this study show the bond behaviour of hybrid FRP-concrete is distinct from that of sole FRP-concrete. The observations were obtained from repeatable tests for each group so that the accuracy of the results was affirmed.

Acknowledgments

The authors acknowledge the financial support from Australian Research Council (ARC LP150100259).

Reference

[1] Teng J, Chen JF, Smith ST, Lam L. Behaviour and strength of FRP-strengthened RC structures: a state-of-the-art review. Proceedings of the institution of civil engineers-structures and buildings. 2003;156:51-62.
[2] Chen JF, Teng J. Anchorage strength models for FRP and steel plates bonded to concrete. Journal of Structural Engineering. 2001;127:784-91.
[3] Teng J, Chen J-F, Smith ST, Lam L. FRP: strengthened RC structures. Frontiers in Physics. 2002:266.

[4] Pham TM, Hao H. Behavior of fiber-reinforced polymer-strengthened reinforced concrete beams under static and impact loads. International Journal of Protective Structures. 2017;8:3-24.
[5] Chen WH, Hong; Jong, Michael; Cui, Jian; Shi, Yanchao; Chen, Li; Pham, Thong M. . Quasi-static and dynamic tensile properties of basalt fibre reinforced polymer. Composites Part B: Engineering. 2017;125:123-33.
[6] Yao M, Zhu D, Yao Y, Zhang H, Mobasher B. Experimental study on basalt FRP/steel single-lap joints under different loading rates and temperatures. Composite Structures. 2016;145:68-79.
[7] Franco A, Royer-Carfagni G. Effective bond length of FRP stiffeners. International Journal of Non-Linear Mechanics. 2014;60:46-57.
[8] Wu Z-M, Hu C-H, Wu Y-F, Zheng J-J. Application of improved hybrid bonded FRP technique to FRP debonding prevention. Construction and Building Materials. 2011;25:2898-905.
[9] Zhang H, Smith ST, Gravina RJ, Wang Z. Modelling of FRP-concrete bonded interfaces containing FRP anchors. Construction and Building Materials. 2017;139:394-402.
[10] Dai J, Ueda T, Sato Y. Development of the nonlinear bond stress–slip model of fiber reinforced plastics sheet–concrete interfaces with a simple method. Journal of Composites for Construction. 2005;9:52-62.
[11] Nakaba K, Kanakubo T, Furuta T, Yoshizawa H. Bond behavior between fiber-reinforced polymer laminates and concrete. Structural Journal. 2001;98:359-67.
[12] Lin J-P, Wu Y-F, Smith ST. Width factor for externally bonded FRP-to-concrete joints. Construction and Building Materials. 2017;155:818-29.
[13] Biolzi L, Ghittoni C, Fedele R, Rosati G. Experimental and theoretical issues in FRP-concrete bonding. Construction and Building Materials. 2013;41:182-90.
[14] Ghorbani M, Mostofinejad D, Hosseini A. Experimental investigation into bond behavior of FRP-to-concrete under mixed-mode I/II loading. Construction and Building Materials. 2017;132:303-12.
[15] Wu Z, Islam S, Said H. A three-parameter bond strength model for frp—concrete interface. Journal of reinforced plastics and composites. 2009;28:2309-23.
[16] Diab HM, Farghal OA. Bond strength and effective bond length of FRP sheets/plates bonded to concrete considering the type of adhesive layer. Composites Part B: Engineering. 2014;58:618-24.
[17] Neubauer U, Rostasy F. Design aspects of concrete structures strengthened with externally bonded CFRP-plates. Proceedings of the seventh international conference on structural faults and repair, 8 July 1997 Volume 2: Concrete and Composites1997.
[18] Ueda T, Dai J. New shear bond model for FRP–concrete interface–from modeling to application. FRP Composites in Civil Engineering-CICE 2004: Proceedings of the 2nd International Conference on FRP Composites in Civil Engineering-CICE 2004, 8-10 December 2004, Adelaide, Australia: Taylor & Francis; 2004. p. 69.
[19] Yuan H, Teng J, Seracino R, Wu Z, Yao J. Full-range behavior of FRP-to-concrete bonded joints. Engineering structures. 2004;26:553-65.
[20] Sato Y KKaKY. Bond behavior between CFRP sheet and concrete (part 1). J Struct Constr Eng AIJ 1997; 500: 75–82. (in Japanese). 1997.
[21] Ko H MS, Palmieri A, et al. Development of a simplified bond stress-slip model for bonded FRP-concrete interfaces. Constr Build Mater 2014; 68: 142–157. 2014.
[22] Carloni C, Santandrea M, Imohamed IAO. Determination of the interfacial properties of SRP strips bonded to concrete and comparison between single-lap and notched beam tests. Engineering Fracture Mechanics. 2017;186:80-104.

[23] Hosseini A, Mostofinejad D. Effective bond length of FRP-to-concrete adhesively-bonded joints: Experimental evaluation of existing models. International Journal of Adhesion and Adhesives. 2014;48:150-8.
[24] Pan J, Leung CK. Effect of concrete composition on FRP/concrete bond capacity. Journal of Composites for Construction. 2007;11:611-8.
[25] Wu Y-F, Jiang C. Quantification of bond-slip relationship for externally bonded FRP-to-concrete joints. Journal of composites for construction. 2013;17:673-86.
[26] Pham TM, Hao H. Impact behavior of FRP-strengthened RC beams without stirrups. Journal of Composites for Construction. 2016;20:04016011.
[27] Nabil F. Grace GA-S, and Wael F. Ragheb. Strengthening of concrete beams using innovative ductile fiber-reinforced polymer fabric. 2002.
[28] Li L-j, Guo Y-c, Huang P-y, Liu F, Deng J, Zhu J. Interfacial stress analysis of RC beams strengthened with hybrid CFS and GFS. Construction and building materials. 2009;23:2394-401.
[29] Choi E, Utui N, Kim HS. Experimental and analytical investigations on debonding of hybrid FRPs for flexural strengthening of RC beams. Composites Part B: Engineering. 2013;45:248-56.
[30] Hawileh RA, Rasheed HA, Abdalla JA, Al-Tamimi AK. Behavior of reinforced concrete beams strengthened with externally bonded hybrid fiber reinforced polymer systems. Materials & Design. 2014;53:972-82.
[31] Mukhtar FM, Faysal RM. A review of test methods for studying the FRP-concrete interfacial bond behavior. Construction and Building Materials. 2018;169:877-87.
[32] Mazzotti C, Savoia M, Ferracuti B. A new single-shear set-up for stable debonding of FRP–concrete joints. Construction and Building Materials. 2009;23:1529-37.
[33] Wan B, Jiang C, Wu Y-F. Effect of defects in externally bonded FRP reinforced concrete. Construction and Building Materials. 2018;172:63-76.
[34] West System. “Epoxy resins and hardeners—Physical properties.” (http://www.westsystem.com/ss/typical-physical-properties) (Jan. 31, 2015). 2015.
[35] ASTM(2008). “Standard test method for tensile properties of polymer matrix composite materials.” ASTM D3039, West Conshohocken, PA. 2008.
[36] Fawzia S, Al-Mahaidi R, Zhao X-L. Experimental and finite element analysis of a double strap joint between steel plates and normal modulus CFRP. Composite structures. 2006;75:156-62.
[37] Manders PW, Bader M. The strength of hybrid glass/carbon fibre composites. Journal of materials science. 1981;16:2233-45.
[38] Aveston J, Sillwood J. Synergistic fibre strengthening in hybrid composites. Journal of Materials Science. 1976;11:1877-83.
[39] Zhang H, Smith ST. Influence of plate length and anchor position on FRP-to-concrete joints anchored with FRP anchors. Composite Structures. 2017;159:615-24.
[40] Yao J, Teng J, Chen JF. Experimental study on FRP-to-concrete bonded joints. Composites Part B: Engineering. 2005;36:99-113.
[41] Pellegrino C, Tinazzi D, Modena C. Experimental study on bond behavior between concrete and FRP reinforcement. Journal of Composites for Construction. 2008;12:180-9.
[42] Woo S-K, Lee Y. Experimental study on interfacial behavior of CFRP-bonded concrete. KSCE Journal of Civil Engineering. 2010;14:385-93.
[43] Lu X, Teng J, Ye L, Jiang J. Bond–slip models for FRP sheets/plates bonded to concrete. Engineering structures. 2005;27:920-37.
[44] Sun W, Peng X, Liu H, Qi H. Numerical studies on the entire debonding propagation process of FRP strips externally bonded to the concrete substrate. Construction and Building Materials. 2017;149:218-35.

[45] Silva MA, Biscaia HC, Marreiros R. Bond–slip on CFRP/GFRP-to-concrete joints subjected to moisture, salt fog and temperature cycles. Composites Part B: Engineering. 2013;55:374-85.
[46] Ouezdou MB, Belarbi A, Bae S-W. Effective bond length of FRP sheets externally bonded to concrete. International Journal of Concrete Structures and Materials. 2009;3:127-31.
[47] Ali-Ahmad M, Subramaniam K, Ghosn M. Experimental investigation and fracture analysis of debonding between concrete and FRP sheets. Journal of engineering mechanics. 2006;132:914-23.
[48] Baldoni J, Lionello G, Zama F, Cristofolini L. Comparison of different filtering strategies to reduce noise in strain measurement with digital image correlation. The Journal of Strain Analysis for Engineering Design. 2016;51:416-30.
[49] Ferracuti B, Savoia M, Mazzotti C. Interface law for FRP–concrete delamination. Composite structures. 2007;80:523-31.
[50] Ali-Ahmad M, Subramaniam K, Ghosn M. Fracture analysis of the debonding between FRP and concrete using digital image correlation. Proceedings of FRAMCOS-5 international conference on fracture of concrete and concrete structures/Vail, Colorado2004. p. 787-93.
[51] Gravina RJ, Aydin H, Visintin P. Extraction and Analysis of Bond-Slip Characteristics in Deteriorated FRP-to-Concrete Joints Using a Mechanics-Based Approach. Journal of Materials in Civil Engineering. 2017;29:04017013.
[52] Instructions for the design, execution and control of strengthening measures through fiber-reinforced composites. Italian Society Research Society 2004; CNR-DT 200/04. 2004.
[53] Dai J, Ueda T, Sato Y. Bonding characteristics of fiber-reinforced polymer sheet-concrete interfaces under dowel load. Journal of Composites for Construction. 2007;11:138-48.
[54] Lu X. Study on FRP-concrete interface. PhD thesis, PRC: Tsinghua Univ; 2004 (in Chinese). 2004.